Electronic Supplementary Information for:

Pseudo-tetrahedral vs pseudo-octahedral Er^{III} single molecule magnets and the disruptive role of coordinated TEMPO radicals

Maria Brzozowska, Gabriela Handzlik, Katarzyna Kurpiewska, Mikołaj Zychowicz and Dawid Pinkowicz*
Jagiellonian University, Faculty of Chemistry, Gronostajowa 2, 30-387 Kraków, Poland

Experimental section

General synthesis considerations

All manipulations were performed under inert gas atmosphere inside an argon filled glovebox (Inert PureLab HE). All solvents used in this study (HPLC grade) were dried under argon using Inert PureSolv EN7 solvent purification system. Anhydrous $ErCl_3$ (at least 99.9%) was purchased from Alfa Aesar and used as received. $Li_3(N_3N)$ was prepared according to the previously published method.[1] Sodium 2,4,6-tri-*tert*-butyl-phenolate (NaTTBP·Et$_2$O) and sodium 2,6-di-*tert*-butyl-4-methylphenolate (NaBHT·Et$_2$O) were prepared by slowly adding dry sodium hydride to the Et$_2$O solution of the respective phenol (Sigma Aldrich, 98%) inside the glovebox. See below for a detailed procedure. NaTTBP·Et$_2$O obtained in this way is identical with that obtained using a slightly different method reported in the literature.[2]

Preparation of sodium 2,4,6-tri-*tert*-butyl-phenolate (NaTTBP·Et$_2$O)

2,4,6-tri-*tert*-butyl-phenol (10.7 g, 40 mmol) was dissolved in 40 ml of dry Et$_2$O (bright yellow solution) and heated to boiling. NaH (0.912 g, 38 mmol) was added in small portions while stirring. Each portion causes vigorous gas evolution. Stirring was continued for another 1.5 h after the last portion of NaH was added. The off-white crystalline precipitate was collected by filtration (the filtrate is yellow) and washed with three portions of Et$_2$O. Yield 10.95 g (80 %). NaTTBP·Et$_2$O obtained in this way is identical with that obtained using a slightly different method reported in the literature.[2]

Preparation of [Er^{III}(TTBP)$_3$(THF)] (1)

NaTTBP·Et$_2$O (3.89 g, 10.9 mmol) and $ErCl_3$ (1.03 g, 3.65 mmol) were suspended in 40 ml of THF. The pink reaction mixture was stirred for 3 days and then the solvent was removed in vacuo. The pink residue was suspended in 50 ml of pentane, stirred for 30 min and then left to settle. Then pink solution was decanted and filtered through a P4 fritted funnel (gravitational filtering). The extraction/filtration was repeated two more times and the pink clear filtrates were combined and left at -40 °C overnight. Large pink crystals were collected from the mixture. Yield: 2.25 g (61 %). The identity and purity of the compound was confirmed by powder X-ray diffraction (PXRD) measurements (Figure S1a).

Preparation of [Er^{III}(TTBP)$_3$(TEMPO)] (2)

Pink solution of **1** (0.213 g, 0.21 mmol) dissolved in 3.0 ml of *n*-pentane was mixed with an orange solution of TEMPO (0.183 g, 1.17 mmol) dissolved in 1.4 ml of the same solvent. The clear dark violet solution was left in an open vial for crystallization. Within 1-2 h the mixture volume was reduced to half of the initial value and violet crystals formed on the bottom. The crystals of **2** were filtered, washed with a quantity of cold *n*-pentane and dried inside the glovebox for 10 min. Yield: 0.040 g (16 %). The identity and purity of the compound was confirmed by powder X-ray diffraction (PXRD) measurements (Figure S1b).

Preparation of [Er^{III}(BHT)$_3$(THF)] (3)

Compound **3** was obtained in an analogous way as **1** by reacting NaBHT·Et$_2$O (7.60 g, 24 mmol) instead of TTBP with $ErCl_3$ (2.00 g, 7.3 mmol) in 100 ml of THF. Yield: 5.01 g (77 %). The identity and purity of the compound was confirmed by powder X-ray diffraction (PXRD) measurements (Figure S1c).

Preparation of [Li(THF)$_2$]$_2$[Er^{III}(N$_3$N)Cl$_2$] (4)

Solid $ErCl_3$ (0.191 g, 0.70 mmol) was added in portions to the THF solution (6.8 ml) of $Li_3(N_3N)$ (0.267 g, 0.71 mmol). The pink turbid reaction mixture became almost clear after stirring overnight. The solution was evaporated to dryness and extracted three times with *n*-pentane (12 ml in total). The pink solution was filtered (P3 fritted glass funnel, gravitational), concentrated down to 3-4 ml and left in the freezer at -40 °C overnight. Pink crystals were collected by filtration. Yield: 49 mg (8 %). The identity and purity of the compound was confirmed by powder X-ray diffraction (PXRD) measurements (Figure S1d).

Single crystal X-ray diffraction (SCXRD)

SCXRD experiments were performed for [Er^{III}(TTBP)$_3$(THF)] (**1**) and [Er^{III}(TTBP)$_3$(TEMPO)] (**2**) using Rigaku XtaLAB Synergy-S (HyPix) and for [Er^{III}(BHT)$_3$(THF)] (**3**) and [Li(THF)$_2$]$_2$[Er^{III}(N$_3$N)Cl$_2$] (**4**) using Bruker D8 Quest Eco (Photon50) diffractometers (Mo Kα radiation, PhotonJet-S microsource in the case of Rigaku and sealed tube Triumph® in the case of Bruker machine). Details of these measurements are gathered in Tables S1 and S2. Single crystals were transferred from the mother liquor into the Paratone-N oil to avoid decomposition and potential solvent loss in contact with ambient atmosphere and mounted using MiTeGen cryomounts. The measurements were performed first at 100 K (full data collection, Table S1) and then near room temperature (fast data collection to avoid crystal decomposition, Table S2) for each crystal. Data processing was performed using CrysAlisPro 1.171.40.67a or Apex3 suite of programs, respectively. The structures were solved using direct methods and refined anisotropically (weighted full-matrix least-squares on F^2 [3,4]). Hydrogen atoms were placed in the calculated positions and refined as riding on the parent atoms. Structural diagrams were prepared using Mercury 2020.2.0 software (CCDC). CCDC 2025204 (**1** at 100 K), 2027594 (**2** at 100 K), 2025203 (**3** at 100 K), 2025202 (**4** at 100 K), 2025205 (**1** at 250 K), 2027595 (**2** at 250 K), 2025200 (**3** at 296 K), 2025201 (**4** at 296 K) contain the supplementary crystallographic data for this paper which can be obtained free of charge from the Cambridge Crystallographic Data Centre via www.ccdc.cam.ac.uk/data_request/cif.

Powder X-ray diffraction (PXRD)

PXRD measurements were performed using Bruker D8 Advance Eco diffractometer equipped with CuKα radiation source and Lynxeye silicon strip detector. The samples were ground using an agate mortar inside the glovebox and loaded into 0.7 mm glass capillaries. The capillaries were broken in half inside the glovebox and their open end was sealed with silicon grease before they were moved to the PXRD instrument. The capillaries were mounted on the goniometer head using wax. The PXRD of each sample was collected in at least three runs in the 2-50 2ϑ range to exclude the possibility of the decomposition of the sample, if the silicon grease seal is not air tight. In each case there were no signs of decomposition within the experiment duration. The experimental PXRD patterns are presented in Figure S1 (colored lines) and compared against the simulated curves (gray lines) obtained from the near-room temperature SCXRD data (the simulated curves were exported using the relevant option of the Mercury 2020.2.0 software).

Magnetic measurements

Magnetic susceptibility measurements were performed using a Quantum Design MPMS-3 Evercool magnetometer in the magnetic fields up to 7 T and 1.8-300 K temperature range. The samples (typically 25-30 mg) was loaded into the custom-made Delrin sample holders[5] inside the glovebox and closed tightly. The experimental data were corrected for the diamagnetism of the sample and the sample holder.

Table S1. Crystal structure solution and refinement parameters for [Er^{III}(TTBP)$_3$(THF)] (**1**), [Er^{III}(TTBP)$_3$(TEMPO)] (**2**), [Er^{III}(BHT)$_3$(THF)] (**3**) and [Li(THF)$_2$]$_2$[Er^{III}(N$_3$N)Cl$_2$] (**4**) at 100 K.

Compound	[Er^{III}(TTBP)$_3$(THF)] (**1**)	[Er^{III}(TTBP)$_3$(TEMPO)] (**2**)	[Er^{III}(BHT)$_3$(THF)] (**3**)	[Li(THF)$_2$]$_2$[Er^{III}(N$_3$N)Cl$_2$] (**4**)
CCDC deposition number	2025204	2027594	2025203	2025202
Formula	C$_{58}$H$_{95}$ErO$_4$	C$_{63}$H$_{105}$ErNO$_4$	C$_{98}$H$_{154}$Er$_2$O$_8$	C$_{31}$H$_{71}$Cl$_2$ErLi$_2$N$_4$O$_4$Si$_3$
M_r/g mol^{-1}	1023.59	1107.73	1794.72	900.23
T/K	100(1)	100(1)	100(1)	100(1)
Crystal system	triclinic	monoclinic	triclinic	monoclinic
Space group	P-1	$P2_1$/n	P-1	$P2_1$/c
a / Å	10.3908(1)	14.12440(10)	14.483(4)	22.9459(19)
b / Å	13.7538(2)	27.2504(3)	18.193(10)	10.0173(8)
c / Å	21.5780(3)	15.9837(2)	19.256(7)	18.5794(15)
α / °	98.962(1)	90	71.753(13)	90
β / °	99.581(1)	90.2240(10)	86.585(10)	89.998(2)
γ / °	109.287(1)	90	81.656(17)	90
V/Å^3	2795.55(7)	6152.01(11)	4767.(3)	4270.6(6)
Z	2	4	2	4
ρ_{calc} / g cm^{-3}	1.216	1.196	1.250	1.400
μ / mm^{-1}	1.542	1.407	1.799	2.210
F(000)	1086	2360	1884	1868
Crystal size / mm^3	0.10 x 0.04 x 0.03	0.12 x 0.06 x 0.04	0.52 x 0.40 x 0.35	0.39 x 0.20 x 0.13
Instrument	Rigaku Synergy S	Rigaku Synergy S	Bruker D8 Quest Eco	Bruker D8 Quest Eco
Radiation	Mo Kα (λ = 0.71073 Å)	Mo Kα (λ = 0.71073 Å)	Mo Kα (λ = 0.71073 Å)	Mo Kα (λ = 0.71073 Å)
2θ range/°	2.241-25.242	2.434-25.242	2.26-25.75	2.31-25.24
Reflections collected	58260	197493	41119	39038
Independent reflections	19074	22437	17791	7719
R_{int}	0.0585	0.0423	0.0762	0.0877
restrains/parameters	0/595	0/653	48/1015	48/461
$R[F_o > 2\sigma(F_o)]$	0.0475	0.0284	0.0499	0.0415
$wR(F^2)$	0.1107	0.0603	0.0960	0.0832
GOF on F^2	1.032	1.041	1.011	1.030
Δρ_{max}, Δρ_{min} /e Å^{-3}	4.648/-2.521	0.991/-0.907	1.268/-1.077	1.568/-1.247
Completeness/%	99.9	99.9	97.4	99.9

Table S2. Crystal structure solution and refinement parameters for $[Er^{III}(TTBP)_3(THF)]$ (**1**), $[Er^{III}(TTBP)_3(THF)]$ (**2**), $[Er^{III}(BHT)_3(TEMPO)]$ (**3**) and $[Li(THF)_2]_2[Er^{III}(N_3N)Cl_2]$ (**4**) near room temperature (250 or 296 K) – structural models obtained for the sole purpose of comparison with the experimental powder X-ray diffraction patterns (see Figure S1 below).

Compound	$[Er^{III}(TTBP)_3(THF)]$ (**1**)	$[Er^{III}(TTBP)_3(TEMPO)]$ (**2**)	$[Er^{III}(BHT)_3(THF)]$ (**3**)	$[Li(THF)_2]_2[Er^{III}(N_3N)Cl_2]$ (**4**)
CCDC deposition number	2025205	2027595	2025200	2025201
Formula	$C_{58}H_{95}ErO_4$	$C_{63}H_{105}ErNO_4$	$C_{49}H_{77}ErO_4$	$C_{31}H_{71}Cl_2ErLi_2N_4O_4Si_3$
M_r/g mol^{-1}	1023.59	1107.73	897.36	900.22
T/K	250(1)	250(1)	296(1)	296(1)
Crystal system	triclinic	monoclinic	triclinic	monoclinic
Space group	P-1	$P2_1/n$	P-1	$P2_1/n$
a / Å	10.4504(2)	14.2971(2)	10.7671(13)	10.2048(16)
b / Å	13.8690(3)	27.4460(5)	12.4225(14)	18.930(3)
c / Å	21.7789(5)	16.0132(2)	19.496(3)	23.147(4)
α / °	98.439(2)	90	74.976(5)	90
β / °	99.276(2)	90.190(2)	77.692(5)	90.010(5)
γ / °	108.951(2)	90	76.963(4)	90
V/Å^3	2878.61(11)	6283.52(16)	2420.3(5)	4471.3(11)
Z	2	4	2	4
ρ_{calc} / g cm^{-3}	1.181	1.171	1.231	1.337
μ / mm^{-1}	1.498	1.378	1.772	2.111
$F(000)$	1086	2360	942	1868
Crystal size / mm^3	0.10 x 0.04 x 0.03	0.12 x 0.06 x 0.04	0.52 x 0.40 x 0.35	0.39 x 0.20 x 0.13
Instrument	Rigaku Synergy S	Rigaku Synergy S	Bruker D8 Quest Eco	Bruker D8 Quest Eco
Radiation	Mo Kα (λ = 0.71073 Å)	Mo Kα (λ = 0.71073 Å)	Mo Kα (λ = 0.71073 Å)	Mo Kα (λ = 0.71073 Å)
2θ range/°	2.230-25.242	2.416-25.242	2.26-25.75	2.267-17.982
Reflections collected	68249	199852	7981	6737
Independent reflections	19831	22878	5102	2742
R_{int}	0.0657	0.0670	0.0626	0.0831
restrains/parameters	0/595	0/653	72/570	60/461
$R[F_o > 2\sigma(F_o)]$	0.0518	0.0400	0.0609	0.0460
$wR(F^2)$	0.1252	0.0885	0.1397	0.1034
GOF on F^2	1.036	1.036	1.072	1.055
$\Delta\rho_{max}$, $\Delta\rho_{min}$ /e Å^{-3}	2.641/-1.686	1.114/-0.801	0.863/-0.861	0.648/-0.445
Completeness/%	99.9	99.9	89.0	89.5

Table S3. Results of the CShM analysis performed using SHAPE software for all Er^{III} central ions in **1**-**4**. Values closer to zero indicate better match with the reference geometry.

	geometry	**1**	**2**	**3** (A)	**3** (B)	**4**
6-vertex polyhedra	D6h Hexagon					33.142
	C5v Pentagonal pyramid					16.834
	Oh Octahedron					**4.980**
	D3h Trigonal prism					9.956
	C5v Johnson pentagonal pyramid					20.017
4-vortex polyhedra	D4h Square	27.369	30.309	29.819	27.941	
	Td Tetrahedron	**1.029**	**0.746**	**0.893**	**1.036**	
	C2v Seesaw	7.722	5.846	8.583	7.857	
	C3v Vacant trigonal bipyramid	2.921	2.182	2.803	2.725	
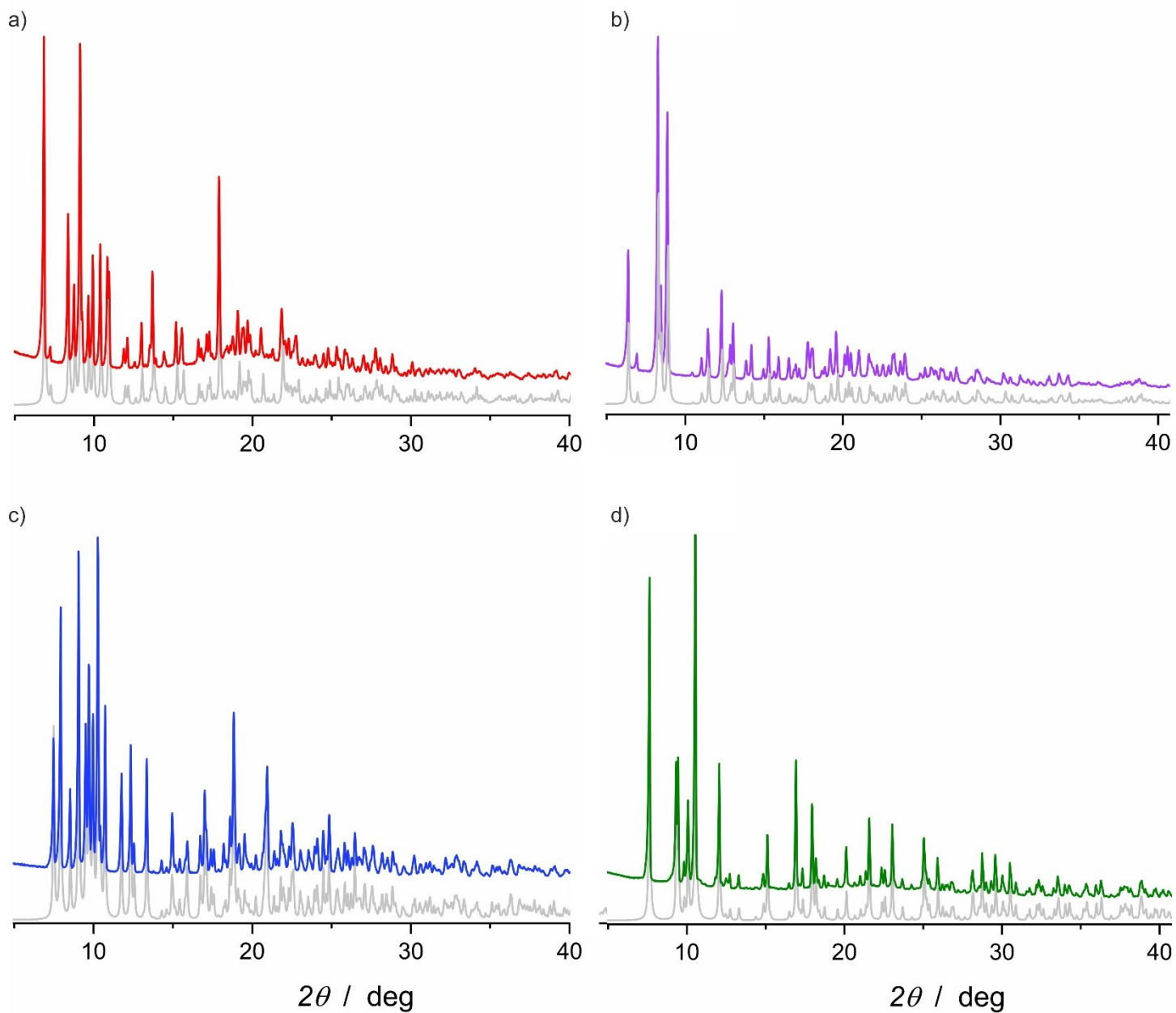
Figure S1. Experimental PXRD patterns for **1** (red line) (a), **2** (violet line) (b), **3** (blue line) (c) and **4** (green line) (d) recorded at room temperature. The grey lines represent the PXRD patterns simulated from room temperature (or 250 K) scXRD data.
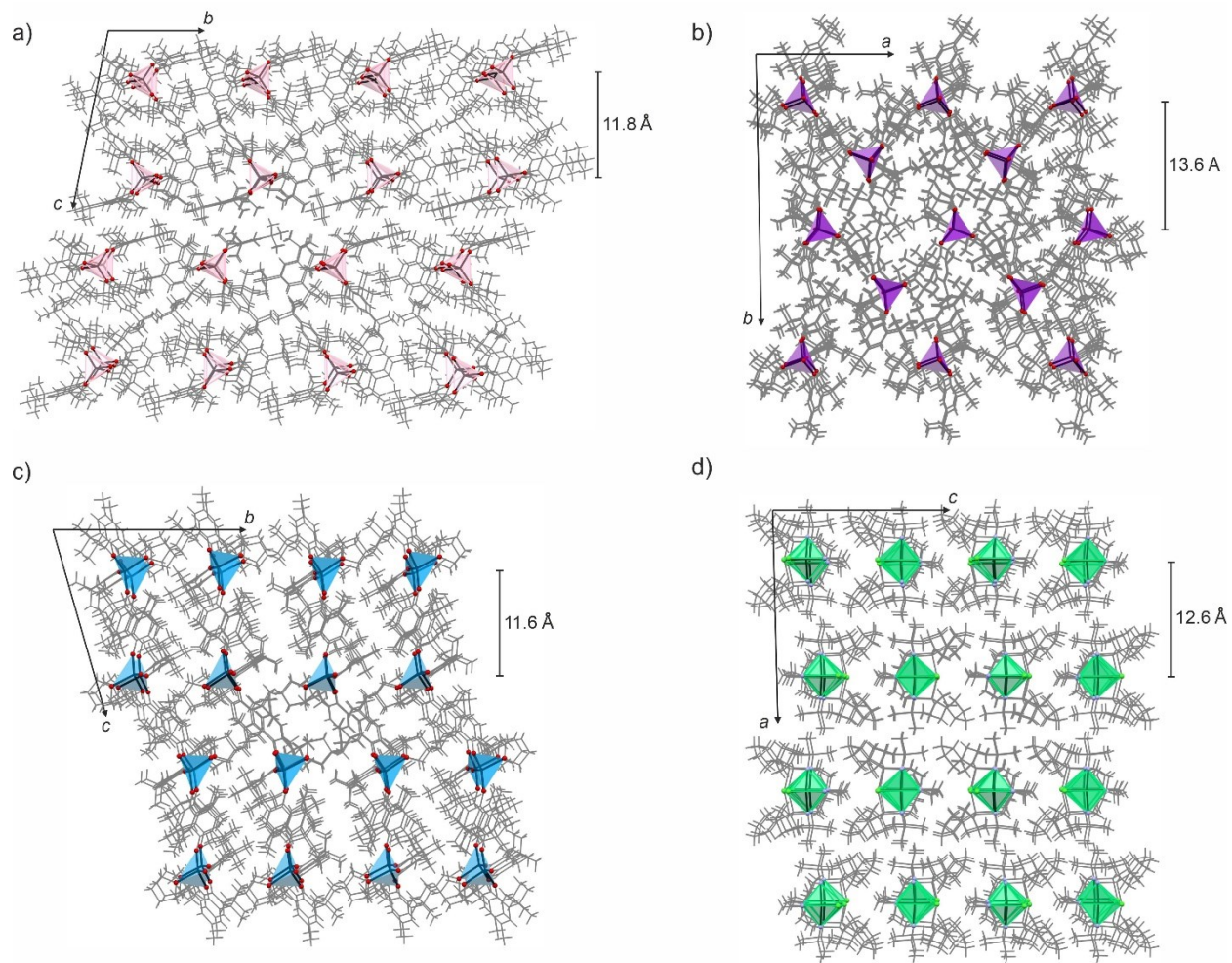
Figure S2. Packing diagrams of **1** (a), **2** (b), **3** (c) and **4** (d) highlighting the 'ErO$_4$' pseudo-tetrahedra (**1**-**3**) and 'ErN$_4$Cl$_2$' pseudo-octahedra (**4**). Organic ligands as well as THF molecules and Li$^+$ cations are drawn as sticks.

Figure S3. DC magnetic properties for compound **1**: $\chi_M T(T)$ recorded at 100 Oe (main plot) and $M(H)$ recorded at 1.8 K (inset). Black points – experimental data, red lines – CASSCF *ab initio* calculations.
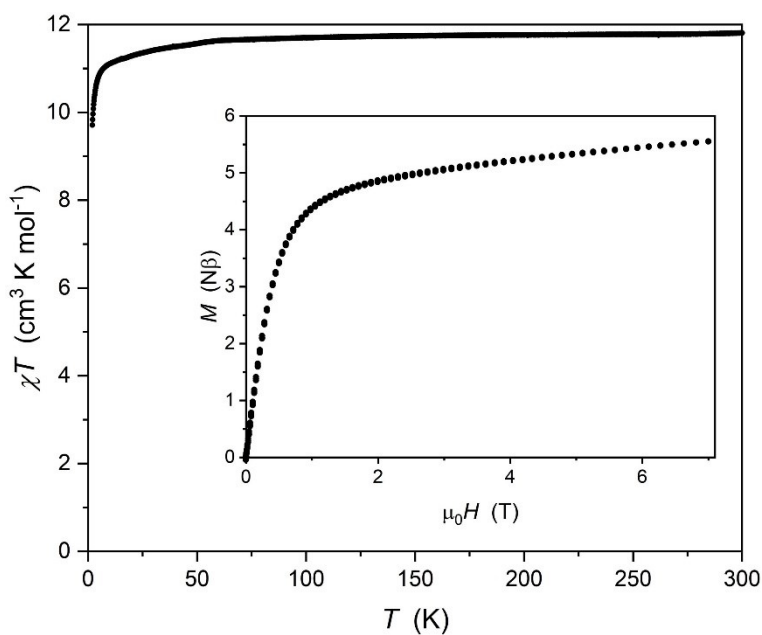
Figure S4. DC magnetic properties for compound **2**: $\chi_M T(T)$ recorded at 100 Oe (main plot) and $M(H)$ recorded at 1.8 K (inset).
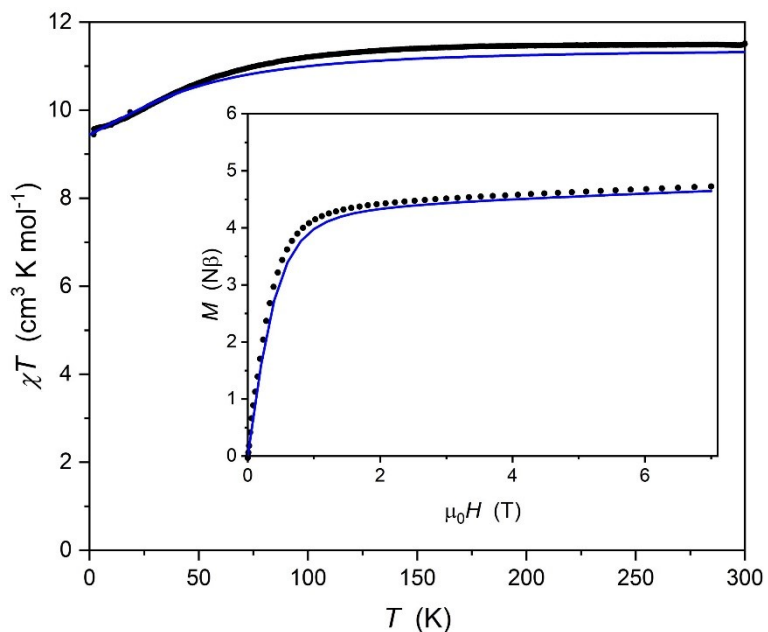
Figure S5. DC magnetic properties for compound **3**: $\chi_M T(T)$ recorded at 100 Oe (main plot) and $M(H)$ recorded at 1.8 K (inset). Black points – experimental data, blue lines – CASSCF *ab initio* calculations.
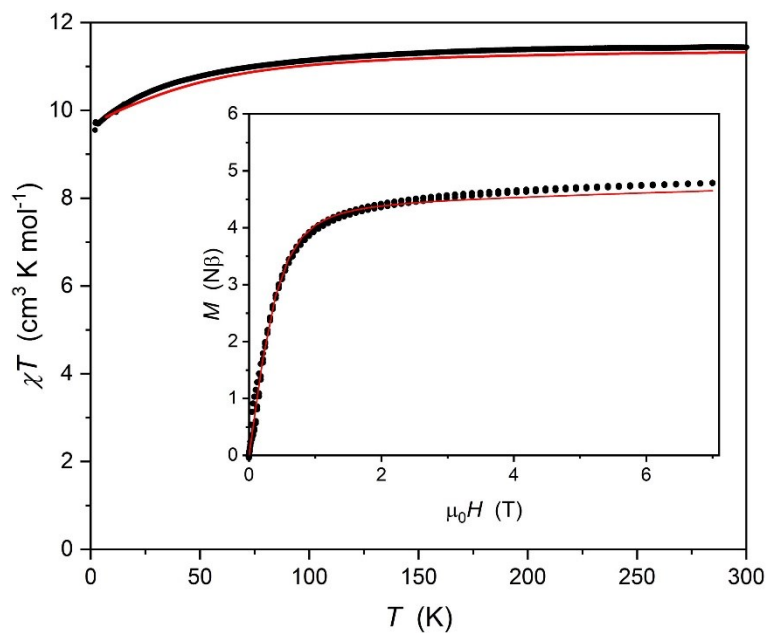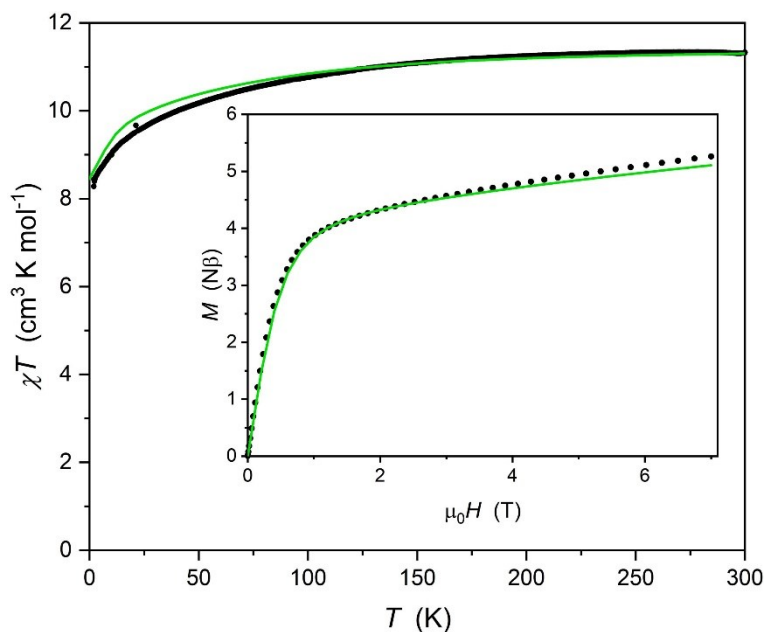

Figure S6. DC magnetic properties for compound **4**: $\chi_M T(T)$ recorded at 100 Oe (main plot) and $M(H)$ recorded at 1.8 K (inset). Black points – experimental data, green lines – CASSCF *ab initio* calculations.
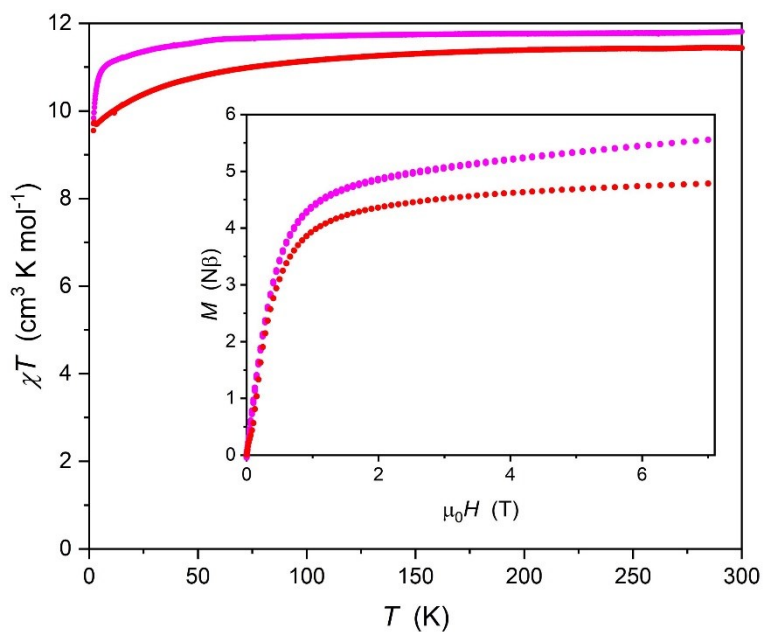
Figure S7. Comparison of the DC magnetic properties for compounds **1** and **2**: $\chi_M T(T)$ recorded at 100 Oe (main plot) and $M(H)$ recorded at 1.8 K (inset). The difference between both curves correspond to the presence of the coordinated TEMPO radical (S = ½) in compound **2**. Experimental $\Delta\chi_M T$ at 300 K is 0.4 cm³·K·mol⁻¹ and ΔM at 70 kOe amounts to 0.77 μ_B while the corresponding values for TEMPO are 0.375 cm³·K·mol⁻¹ and 1.00 μ_B.

AC magnetic properties of compound 1 (Section AC1)

Frequency dependence of the out-of-phase magnetic susceptibility (χ'') of **1** at 1.8 K shows two maxima in the 1-1000 Hz range under 100 and 200 Oe applied DC field, but only the low frequency one is analysed further (Table S4 and Figure S8a). This maximum shifts with magnetic field from around 20 Hz at 100 Oe to around 9 Hz at 1000 Oe and then again to higher frequencies above 3000 Oe. Contributions from the QTM and the direct process have been identified in the low- and high-field ranges of the $\tau(H)$ dependence (Figure 3a), respectively. Fitting of the $\tau(H)$ dependence using Eq. 2 resulted in best-fit parameters A_1, A_2, A_3 and A_4 which were used to calculate parameters for the temperature dependence: $A = 2298$ s^{-1} and $B_2 = 0$ s$^{-1}\cdot$K^{-1} at 0 Oe applied field and $A = 0.46$ s^{-1} and $B_2 = 3.7\cdot10^{-3}$ s$^{-1}\cdot$K^{-1} at 1000 Oe applied field in Eq. 3. The temperature dependence of the AC magnetic susceptibility was measured at 0 Oe (Figure S8b) and at 1000 Oe (optimum field; Figure S8c) in order to analyze both temperature dependences simultaneously. The χ'' maximum is visible up to 10.1 K at 0 Oe and up to 11.2 K at 1000 Oe in the 1 - 1000 Hz window. At 0 Oe the $\chi''(\nu)$ maximum does not move with temperature up to 6.8 K (Figure S8b). Simultaneous fitting of the temperature dependences of ln(τ) at 0 and 1000 Oe using Eq. 3 (see main text) with A and B_2 fixed (based on the $\tau(H)$ dependence fitting), shows a significant contribution of the Raman relaxation process ($C = 1.3(1)\cdot10^{-4}$ s$^{-1}\cdot$K^{-2} assuming fixed exponent $n = 7$ which is not typical for Kramers ions and might indicate a more complex Raman relaxation mechanism involving a vibronic barrier;[6,7] note that reasonable fits could only be obtained when n was close to 7) and Orbach relaxation process ($\tau_0 = 1.4(5)\cdot10^{-6}$ s; $U_{eff}/k_B = 63(4)$ K) (Figure 3b). All parameters obtained by fitting the respective relaxation rates vs magnetic field and temperature using Eqs 2 and 3 are collected in Table S5 and Table 3 in the main text.

Table S4. Values of α and τ parameters (uncertainties provided in parentheses) obtained from generalized Debye model fitting of the $\tau(\nu)$ dependences for **1** at 6.0 K measured in the 0-18000 Oe magnetic field range (columns 1-5), at 0 Oe in the 1.8-10.1 K temperature range (columns 6-10) and at 1000 Oe in the 4.2-11.7 K temperature range (columns 11-15).

| | Figure S8a | | | | | Figure S8b | | | | | Figure S8c | | | |
| | T = 6.0 K | | | | | H = 0 Oe | | | | | H = 1000 Oe | | | |
H (Oe)	χ_s (cm$^3\cdot$mol^{-1})	χ_t (cm$^3\cdot$mol^{-1})	α	τ (s)	T (K)	χ_s (cm$^3\cdot$mol^{-1})	χ_t (cm$^3\cdot$mol^{-1})	α	τ (s)	T (K)	χ_s (cm$^3\cdot$mol^{-1})	χ_t (cm$^3\cdot$mol^{-1})	α	τ (s)
0	0.42(1)	1.68(1)	0.104(7)	4.25(4)·10^{-4}	1.8	1.41(8)	5.33(4)	0.094(20)	6.13(22)·10^{-4}	4.2	0.342(1)	2.42(1)	0.042(3)	3.26(3)·10^{-1}
100	1.14(2)	1.66(1)	0.024(20)	1.07(3)·10^{-2}	2.0	1.26(7)	4.77(3)	0.096(19)	5.97(20)·10^{-4}	4.4	0.331(1)	2.30(1)	0.035(2)	2.16(1)·10^{-1}
200	0.77(1)	1.67(1)	0.016(7)	1.32(1)·10^{-2}	2.2	1.16(6)	4.35(3)	0.097(17)	5.86(19)·10^{-4}	4.6	0.321(1)	2.189(6)	0.028(2)	1.47(1)·10^{-1}
300	0.45(1)	1.71(2)	0.128(17)	1.34(4)·10^{-2}	2.4	1.08(5)	4.01(2)	0.097(16)	5.76(17)·10^{-4}	4.8	0.313(1)	2.096(4)	0.024(2)	1.03(1)·10^{-1}
400	0.37(1)	1.68(1)	0.064(8)	1.54(2)·10^{-2}	2.6	0.99(4)	3.71(2)	0.102(14)	5.57(15)·10^{-4}	5.0	0.304(1)	2.012(4)	0.022(2)	7.37(2)·10^{-2}
500	0.324(3)	1.66(1)	0.038(5)	1.65(1)·10^{-2}	2.9	0.87(3)	3.35(1)	0.108(10)	5.29(11)·10^{-4}	5.2	0.295(1)	1.935(3)	0.019(2)	5.38(2)·10^{-2}
600	0.299(2)	1.663(3)	0.027(3)	1.70(1)·10^{-2}	3.2	0.78(2)	3.058(7)	0.113(7)	5.03(7)·10^{-4}	5.4	0.287(1)	1.865(2)	0.018(2)	3.99(1)·10^{-2}
700	0.282(3)	1.652(2)	0.013(5)	1.75(1)·10^{-2}	3.5	0.70(1)	2.809(5)	0.119(6)	4.83(6)·10^{-4}	5.6	0.279(1)	1.803(2)	0.018(2)	3.01(1)·10^{-2}
1000	0.266(1)	1.648(2)	0.014(2)	1.76(1)·10^{-2}	3.8	0.64(1)	2.597(4)	0.121(5)	4.70(5)·10^{-4}	5.9	0.269(1)	1.713(2)	0.015(1)	2.00(1)·10^{-2}
1500	0.258(1)	1.631(3)	0.011(2)	1.75(1)·10^{-2}	4.1	0.60(1)	2.415(3)	0.122(4)	4.63(4)·10^{-4}	6.2	0.261(1)	1.632(2)	0.013(1)	1.37(1)·10^{-2}
2000	0.255(2)	1.614(3)	0.013(3)	1.74(1)·10^{-2}	4.4	0.56(1)	2.255(3)	0.123(5)	4.56(5)·10^{-4}	6.5	0.252(1)	1.559(1)	0.010(2)	9.60(2)·10^{-3}
2500	0.258(3)	1.588(6)	0.011(5)	1.72(1)·10^{-2}	4.7	0.53(1)	2.116(3)	0.122(5)	4.51(5)·10^{-4}	6.8	0.245(1)	1.494(1)	0.009(2)	6.86(2)·10^{-3}
3000	0.249(1)	1.562(2)	0.018(2)	1.68(1)·10^{-2}	5.0	0.50(1)	1.993(3)	0.121(5)	4.47(5)·10^{-4}	7.1	0.237(1)	1.434(1)	0.008(2)	4.97(1)·10^{-3}
3500	0.245(2)	1.533(3)	0.025(3)	1.63(1)·10^{-2}	5.3	0.48(1)	1.884(3)	0.119(5)	4.41(5)·10^{-4}	7.4	0.231(1)	1.378(1)	0.007(2)	3.66(1)·10^{-3}
4000	0.243(1)	1.500(2)	0.027(2)	1.56(1)·10^{-2}	5.6	0.46(1)	1.787(3)	0.117(5)	4.34(5)·10^{-4}	7.7	0.225(1)	1.327(1)	0.007(2)	2.73(1)·10^{-3}
4500	0.240(1)	1.462(2)	0.030(2)	1.47(1)·10^{-2}	5.9	0.45(1)	1.698(3)	0.111(5)	4.30(5)·10^{-4}	8.0	0.219(2)	1.280(1)	0.006(2)	2.06(1)·10^{-3}
5000	0.235(2)	1.424(3)	0.040(3)	1.38(1)·10^{-2}	6.2	0.43(1)	1.618(2)	0.105(5)	4.21(5)·10^{-4}	8.3	0.214(2)	1.235(1)	0.005(2)	1.57(1)·10^{-3}
5500	0.231(1)	1.385(2)	0.044(3)	1.27(1)·10^{-2}	6.5	0.42(1)	1.545(2)	0.098(5)	4.10(4)·10^{-4}	8.6	0.211(2)	1.194(1)	0.002(2)	1.21(1)·10^{-3}
6000	0.226(2)	1.342(3)	0.054(3)	1.16(1)·10^{-2}	6.8	0.40(1)	1.479(2)	0.091(5)	3.95(4)·10^{-4}	8.9	0.210(5)	1.156(2)	0.000(6)	9.50(8)·10^{-4}
7000	0.215(2)	1.253(3)	0.075(4)	9.32(6)·10^{-3}	7.1	0.395(7)	1.418(2)	0.082(5)	3.79(4)·10^{-4}	9.2	0.203(3)	1.119(1)	0.000(3)	7.45(4)·10^{-4}
8000	0.202(3)	1.163(4)	0.101(5)	7.23(7)·10^{-3}	7.4	0.40(1)	1.365(4)	0.077(10)	3.63(7)·10^{-4}	9.7	0.206(4)	1.064(1)	0.000(4)	5.14(3)·10^{-4}
9000	0.188(4)	1.073(4)	0.130(7)	5.48(7)·10^{-3}	7.7	0.380(7)	1.309(2)	0.057(5)	3.44(4)·10^{-4}	10.2	0.212(7)	1.014(2)	0.000(7)	3.63(4)·10^{-4}
10000	0.173(5)	0.986(4)	0.161(9)	4.09(7)·10^{-3}	8.0	0.373(6)	1.261(2)	0.045(5)	3.22(3)·10^{-4}	10.7	0.22(1)	0.969(2)	0.000(9)	2.62(4)·10^{-4}
11000	0.157(6)	0.902(5)	0.191(11)	3.02(7)·10^{-3}	8.3	0.367(7)	1.217(2)	0.033(5)	2.98(3)·10^{-4}	11.2	0.25(2)	0.928(2)	0.000(13)	1.95(6)·10^{-4}
12000	0.140(7)	0.826(5)	0.223(13)	2.24(6)·10^{-3}	8.6	0.362(7)	1.175(1)	0.021(5)	2.75(3)·10^{-4}	11.7	0.29(2)	0.891(2)	0.000(18)	1.53(7)·10^{-4}
13000	0.14(1)	0.774(6)	0.252(18)	1.69(7)·10^{-3}	8.9	0.359(7)	1.137(1)	0.009(6)	2.51(10)·10^{-4}					
14000	0.10(1)	0.688(5)	0.284(16)	1.22(5)·10^{-3}	9.2	0.34(2)	1.099(4)	0.000(19)	2.32(3)·10^{-4}					
15000	0.08(1)	0.633(5)	0.318(21)	9.11(6)·10^{-4}	9.5	0.35(1)	1.068(1)	0.000(7)	2.05(3)·10^{-4}					
16000	0.06(2)	0.581(5)	0.350(23)	6.72(5)·10^{-4}	9.8	0.34(1)	1.037(1)	0.000(8)	1.82(4)·10^{-4}					
17000	0.05(2)	0.527(5)	0.369(24)	4.96(5)·10^{-4}	10.1	0.34(1)	1.008(1)	0.000(9)	1.62(4)·10^{-4}					
18000	0.02(3)	0.488(5)	0.419(28)	3.45(5)·10^{-4}										

Figure S8. In-phase (χ') and out-of-phase (χ'') AC susceptibilities for **1** at 6.0 K measured in the 0-18000 Oe magnetic field range (a), at 0 Oe in the 1.8-10.1 K temperature range (b) and at 1000 Oe in the 4.1-11.7 K temperature range (c). Values of α and τ parameters are gathered in Table S4. The solid lines are the best fits to generalized Debye model.

Table S5. Values of the best-fit parameters obtained by fitting the $\tau^{-1}(H)$ using Eq. 2 (top part of the table) and the $\tau(T)$ using Eq. 3 (bottom part of the table) for compound **1**. The relevant fits are shown in Figure 3a and 3b in the main text, respectively. This table is also included in Table 3 in the main text.

$$\tau^{-1}(H) = A_1/(1+A_2H^2) + B_1H^4 + D \qquad\qquad\qquad \text{(Eq. 2)}$$

$$\ln\tau(T^{-1}) = \ln[(A + B_2T + CT^n + \tau_0^{-1}\exp(-U_{eff}/k_BT))^{-1}] \qquad \text{(Eq. 3)}$$

T (K)	6.0	
range (Hz)	1-1000	
field range (Oe)	0-18000	
A_1 (s^{-1})	2298(118)	
A_2 (Oe^{-2})	5(3)·10^{-3}	
B_1 (Oe^{-4})	2.23(6)·10^{-14}	
D (s^{-1})	56(5)	
R^2	0.98511	
H_{DC} (Oe)	0	1000
range (Hz)	1-1000	1-1000
temp. range (K)	1.8-10.1	1.8-10.1
A (s^{-1})	2298 (fixed)	0.46 (fixed)
B_2 (s^{-1}K^{-1})	0 (fixed)	3.7·10^{-3} (fixed)
C (s^{-1}K^{-n})	1.3(1)·10^{-4}	
n	7 (fixed)	7 (fixed)
τ_0 (s)	1.4(5)·10^{-6}	
(U_{eff}/k_B) (K)	63(4)	
R^2	0.99843	

AC magnetic properties of compound 2 (Section AC2)

The AC magnetic susceptibility for compound **2** does not show any frequency dependence as evidenced by the $\chi',\chi''(T)$ plots performed at 7, 70 and 700 Hz (Figure S9).
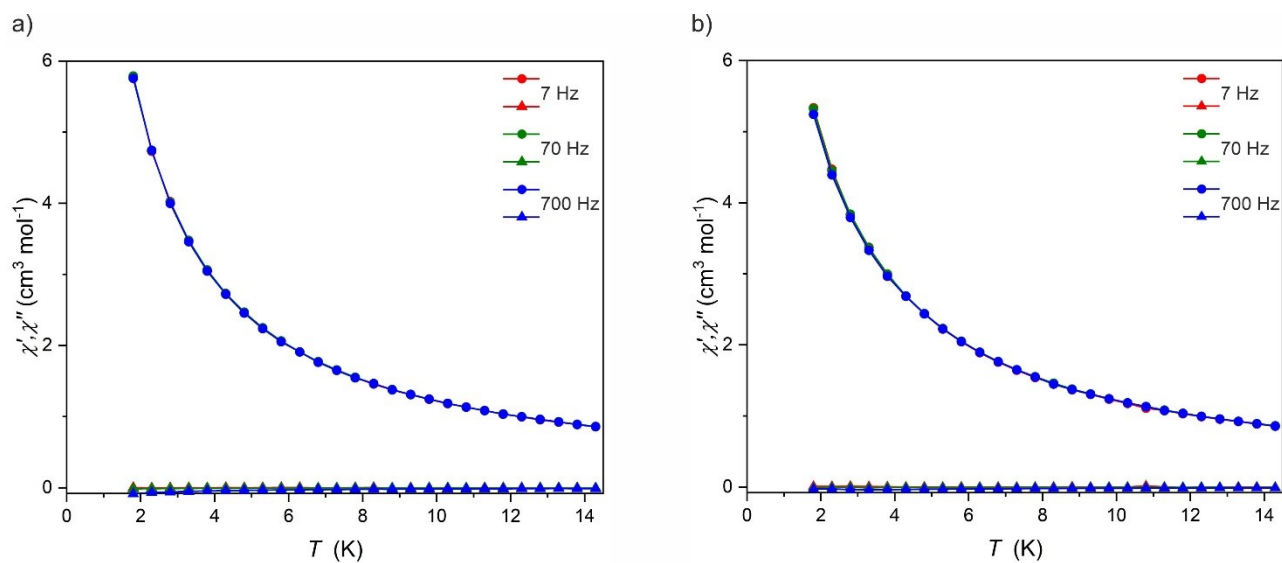
Figure S9. Temperature dependence of the in-phase (χ') and out-of-phase (χ'') AC susceptibilities using 7, 70 and 700 Hz frequency for compound **2** measured at 0 (a) and 1000 Oe (b) external magnetic field.

AC magnetic properties of compound 3 (Section AC3)

Similarly to **1**, the frequency dependence of the out-of-phase magnetic susceptibility (χ'') of **3** at 1.8 K shows two maxima in the 1-1000 Hz range under 100 and 200 Oe applied DC field, but only the low frequency one is analysed further (Table S6 and Figure S10a). This maximum shifts with magnetic field from around 15 Hz at 100 Oe to around 6 Hz at 1500 Oe and then again to higher frequencies above 3500 Oe. Contributions from the QTM and the direct process have been identified in the low- and high-field ranges of the $\tau(H)$ dependence (Figure 3c), respectively. Fitting of the $\tau(H)$ dependence using Eq. 2 resulted in best-fit parameters A_1, A_2, A_3 and A_4 which were used to calculate parameters for the temperature dependence: $A = 3096$ s^{-1} and $B_2 = 0$ s^{-1}·K^{-1} at 0 Oe applied field and $A = 0.20$ s^{-1} and $B_2 = 0.3$ s^{-1}·K^{-1} at 1000 Oe applied field in Eq. 3. The temperature dependence of the AC magnetic susceptibility was measured at 0 Oe (Figure S10b) and at 1500 Oe (optimum field; Figure S10c) in order to analyze both temperature dependences simultaneously. The χ'' maximum is visible up to 6.5 K at 0 Oe and up to 8.0 K at 1500 Oe in the 1 - 1000 Hz window. At 0 Oe the $\chi''(\nu)$ maximum does not move with temperature up to 5.8 K (Figure S10b). Simultaneous fitting of the temperature dependences of ln(τ) at 0 and 1500 Oe using Eq. 3 (see main text) with A and B_2 fixed (based on the $\tau(H)$ dependence fitting), shows a significant contribution of the Raman relaxation process ($C = 1.5(1) \cdot 10^{-3}$ s^{-1}·K^{-2}, assuming fixed exponent $n = 7$ which is not typical for Kramers ions and might indicate a more complex Raman relaxation mechanism involving a vibronic barrier;[6,7] note that reasonable fits could only be obtained when n was close to 7) and Orbach relaxation process ($\tau_0 = 7(3) \cdot 10^{-7}$ s; $U_{eff}/k_B = 48(3)$ K) (Figure 3d). All parameters obtained by fitting the respective relaxation rates vs magnetic field and temperature using Eqs 2 and 3 are collected in Table S7 and in Table 3 in the main text.

Table S6. Values of α and τ parameters (uncertainties provided in parentheses) obtained from generalized Debye model fitting of the $\tau(\nu)$ dependences for **3** at 4.0 K measured in the 0-16000 Oe magnetic field range (columns 1-5), at 0 Oe in the 1.8-7.7 K temperature range (columns 6-10) and at 1000 Oe in the 3-8.0 K temperature range (columns 1-15).

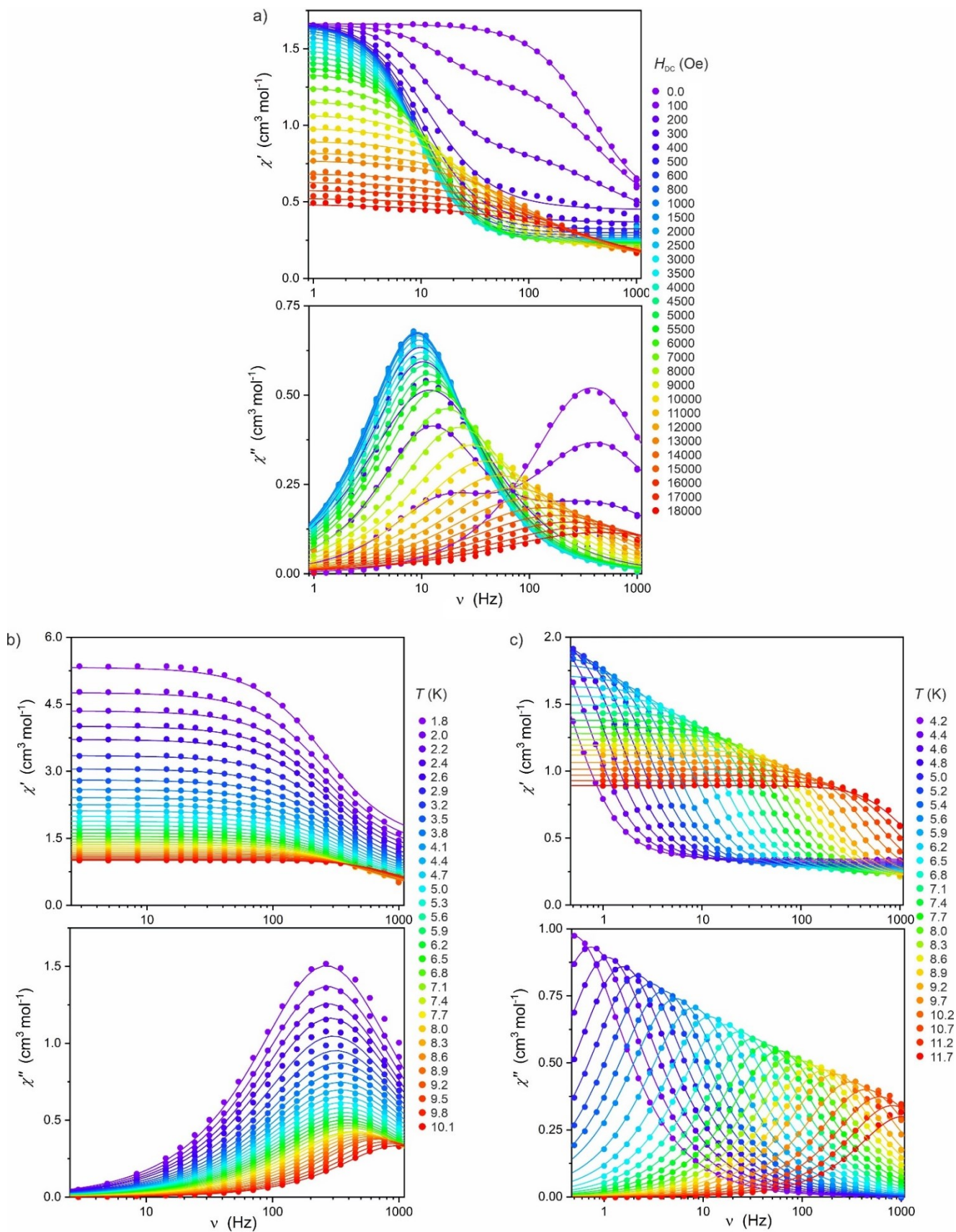| Figure S10a					Figure S10b					Figure S10c				
T = 4.0 K					H = 0 Oe					H = 1500 Oe				
H (Oe)	χ_s (cm^3·mol^{-1})	χ_t (cm^3·mol^{-1})	α	τ (s)	T (K)	χ_s (cm^3·mol^{-1})	χ_t (cm^3·mol^{-1})	α	τ (s)	T (K)	χ_s (cm^3·mol^{-1})	χ_t (cm^3·mol^{-1})	α	τ (s)
0	0.52(1)	2.456(3)	0.080(5)	3.19(3)·10^{-4}	3.2	0.63(2)	5.52(1)	0.092(5)	3.27(4)·10^{-4}	3.0	0.116(1)	3.07(4)	0.090(4)	2.64(5)·10^{-1}
100	1.74(2)	2.460(6)	0.090(50)	1.44(13)·10^{-2}	3.5	0.58(2)	4.91(1)	0.091(6)	3.24(4)·10^{-4}	3.2	0.109(1)	2.87(2)	0.089(3)	1.57(1)·10^{-1}
200	1.10(1)	2.462(6)	0.090(12)	1.69(3)·10^{-2}	3.8	0.54(2)	4.481(6)	0.087(6)	3.22(4)·10^{-4}	3.4	0.099(2)	2.75(1)	0.097(3)	9.86(8)·10^{-2}
300	0.64(1)	2.471(6)	0.090(6)	2.01(2)·10^{-2}	4.1	0.51(2)	4.119(6)	0.083(6)	3.16(4)·10^{-4}	3.6	0.094(3)	2.65(1)	0.105(3)	6.35(5)·10^{-2}
400	0.36(1)	2.479(6)	0.094(3)	2.28(1)·10^{-2}	4.4	0.48(2)	3.808(5)	0.077(6)	3.09(4)·10^{-4}	3.8	0.086(3)	2.53(1)	0.110(4)	4.12(3)·10^{-2}
500	0.211(4)	2.49(1)	0.120(4)	2.45(2)·10^{-2}	4.7	0.46(1)	3.420(5)	0.069(6)	2.97(4)·10^{-4}	4.0	0.080(4)	2.43(1)	0.116(4)	2.73(2)·10^{-2}
600	0.162(3)	2.480(7)	0.113(3)	2.58(1)·10^{-2}	5.0	0.44(1)	3.104(5)	0.058(6)	2.83(4)·10^{-4}	4.2	0.075(4)	2.316(8)	0.118(4)	1.85(1)·10^{-2}
800	0.116(3)	2.459(7)	0.109(3)	2.70(1)·10^{-2}	5.3	0.43(1)	2.842(4)	0.044(6)	2.66(3)·10^{-4}	4.4	0.071(4)	2.216(6)	0.118(4)	1.28(1)·10^{-2}
1000	0.098(3)	2.440(8)	0.109(3)	2.74(2)·10^{-2}	5.6	0.42(1)	2.620(4)	0.029(6)	2.45(3)·10^{-4}	4.6	0.066(4)	2.124(6)	0.121(4)	9.00(6)·10^{-3}
1500	0.080(4)	2.38(1)	0.111(4)	2.70(2)·10^{-2}	5.9	0.41(1)	2.431(4)	0.014(6)	2.24(3)·10^{-4}	4.8	0.062(5)	2.042(6)	0.126(4)	6.47(5)·10^{-3}
2000	0.084(7)	2.30(2)	0.110(8)	2.60(4)·10^{-2}	6.2	0.41(1)	2.267(4)	0.000(6)	2.01(3)·10^{-4}	5.0	0.058(5)	1.964(5)	0.127(4)	4.73(4)·10^{-3}
2500	0.069(4)	2.24(1)	0.130(5)	2.43(2)·10^{-2}	6.5	0.41(2)	2.124(3)	0.000(8)	1.79(4)·10^{-4}	5.3	0.050(7)	1.860(6)	0.134(5)	3.07(3)·10^{-3}
3000	0.064(4)	2.14(1)	0.137(5)	2.19(2)·10^{-2}	6.8	0.40(2)	1.997(3)	0.00(1)	1.55(4)·10^{-4}	5.6	0.043(8)	1.766(6)	0.139(6)	2.05(2)·10^{-3}
3500	0.049(6)	2.04(1)	0.157(7)	1.89(3)·10^{-2}	7.1	0.40(3)	1.885(3)	0.00(1)	1.36(5)·10^{-4}	5.9	0.04(1)	1.681(5)	0.146(7)	1.41(2)·10^{-3}
4000	0.053(6)	1.91(1)	0.020(33)	8.57(67)·10^{-3}	7.4	0.44(4)	1.784(2)	0.00(2)	1.23(7)·10^{-4}	6.2	0.03(1)	1.603(5)	0.150(7)	9.92(14)·10^{-4}
4500	0.044(7)	1.80(1)	0.020(36)	7.05(43)·10^{-3}	7.7	0.47(5)	1.693(2)	0.00(2)	1.11(9)·10^{-4}	6.5	0.04(1)	1.533(5)	0.153(8)	7.21(11)·10^{-4}
5000	0.03(1)	1.67(1)	0.049(36)	5.86(35)·10^{-3}						6.8	0.05(1)	1.467(5)	0.149(9)	5.43(10)·10^{-4}
5500	0.02(1)	1.56(2)	0.061(24)	4.47(18)·10^{-3}						7.1	0.08(2)	1.406(4)	0.143(9)	4.23(9)·10^{-4}
6000	0.00(1)	1.45(2)	0.074(24)	3.41(13)·10^{-3}						7.4	0.13(2)	1.351(4)	0.127(10)	3.47(8)·10^{-4}
7000	0.00(2)	1.23(2)	0.096(15)	1.94(5)·10^{-3}						7.7	0.19(2)	1.299(3)	0.106(9)	2.96(6)·10^{-4}
8000	0.00(3)	1.03(2)	0.104(15)	1.10(3)·10^{-3}						8.0	0.25(1)	1.250(2)	0.083(8)	2.56(5)·10^{-4}
9000	0.00(4)	0.88(2)	0.107(38)	6.51(33)·10^{-4}										
10000	0.00(6)	0.75(2)	0.133(30)	4.19(16)·10^{-4}										
11000	0.00(8)	0.65(2)	0.149(54)	2.84(22)·10^{-4}										
12000	0.00(11)	0.58(3)	0.221(31)	1.91(12)·10^{-4}										
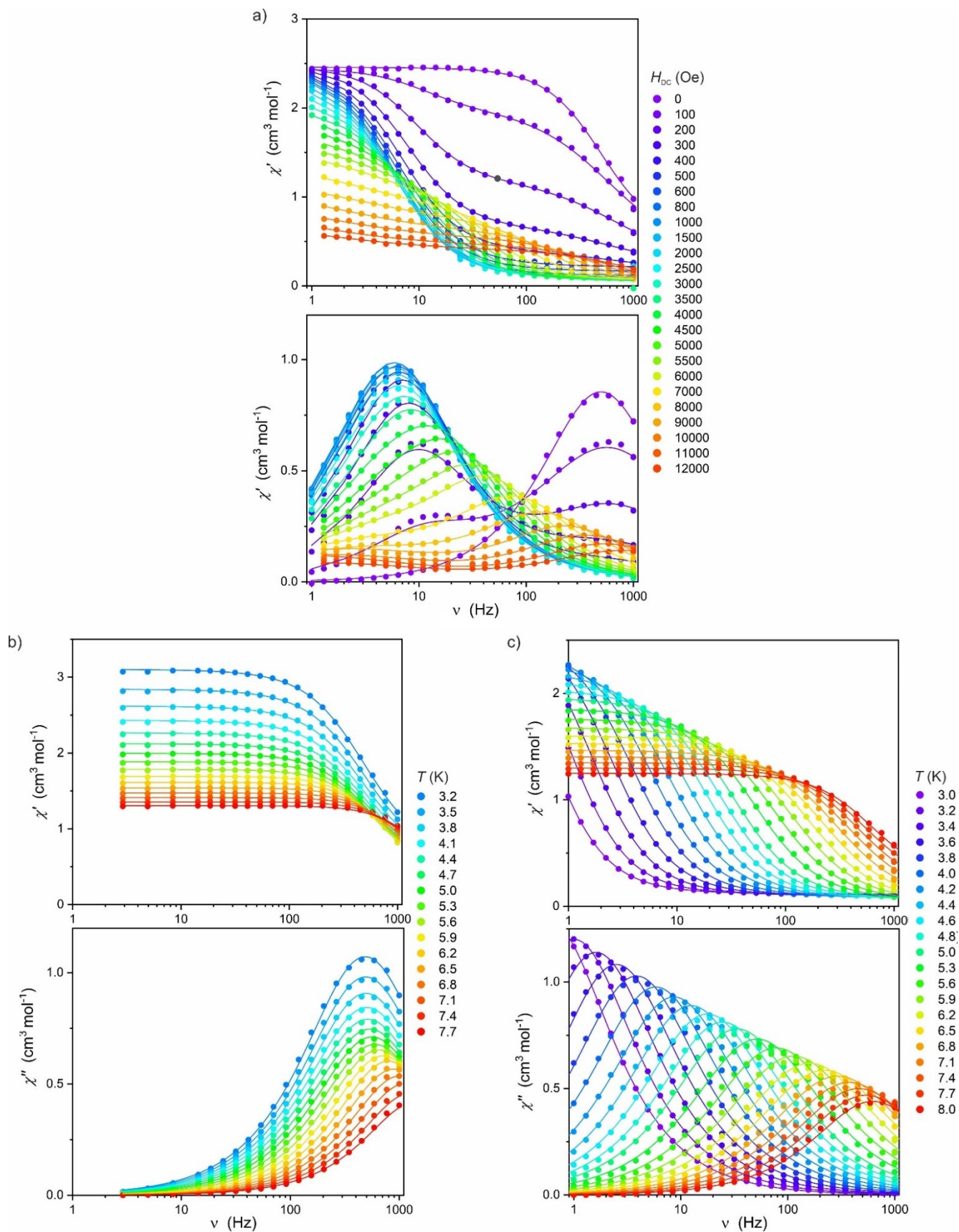
Figure S10. In-phase (χ') and out-of-phase (χ'') AC susceptibilities for **3** at 4.0 K measured in the 0-12000 Oe magnetic field range (a), at 0 Oe in the 3.2-7.7 K temperature range (b) and at 1500 Oe in the 3.0-8.0 K temperature range (c). Values of α and τ parameters are gathered in Table S6. The solid lines are the best fits to generalized Debye model.

Table S7. Values of the best-fit parameters obtained by fitting the $\tau^{-1}(H)$ using Eq. 2 (top part of the table) and the $\tau(T)$ using Eq. 3 (bottom part of the table) for compound **3**. The relevant fits are shown in Figure 3c and 3d in the main text, respectively. This table is also included in Table 3 in the main text.

$\tau^{-1}(H) = A_1/(1+A_2H^2) + B_1H^4 + D$ (Eq. 2)

$\ln\tau(T^{-1}) = \ln[(A + B_2T + CT^n + \tau_0^{-1}\exp(-U_{\text{eff}}/k_BT))^{-1}]$ (Eq. 3)

T (K)	4.0	
range (Hz)	1-1000	
field range (Oe)	0-12000	
A_1 (s^{-1})	3096(104)	
A_2 (Oe^{-2})	$7(3)\cdot10^{-3}$	
B_1 (Oe^{-4})	$2.36(4)\cdot10^{-13}$	
D (s^{-1})	34(4)	
R^2	0.99569	
H_{DC} (Oe)	0	1500
range (Hz)	1-1000	1-1000
temp. range (K)	3.2-7.7	3.0-8.0
A (s^{-1})	3096 (fixed)	0.20 (fixed)
B_2 (s^{-1}K^{-1})	0 (fixed)	$3.0\cdot10^{-1}$ (fixed)
C (s^{-1}K^{-n})		$1.5(1)\cdot10^{-3}$
n	7 (fixed)	7 (fixed)
τ_0 (s)		$7(3)\cdot10^{-7}$
(U_{eff}/k_B) (K)		48(3)
R^2		0.99818

AC magnetic properties of compound 4 (Section AC4)

Frequency dependence of the out-of-phase magnetic susceptibility (χ'') of **4** shows a single maximum in the 18.6-1000 Hz range under small applied DC field (T = 1.8 K; Table S8 and Figure S11a). This χ'' maximum shifts with the magnetic field from around 850 Hz at 200 Oe to around 100 Hz at 2000 Oe (optimum field) and then again to higher frequencies in the 2000-4500 Oe range. Contributions from the QTM and the direct process have been identified in the low- and high-field ranges of the $\tau(H)$ dependence (Figure 3e), respectively. Fitting of the $\tau(H)$ dependence using Eq. 2 resulted in best-fit parameters A_1, A_2, A_3 and A_4 which were used to calculate parameters: A = 157.6 s^{-1} and B_2 = 63.1 s$^{-1}\cdot$K^{-1} in Eq. 3. The temperature dependence of the AC magnetic susceptibility was measured at the optimum DC field of 2000 Oe in order to analyze the temperature dependence of the relaxation process in a possibly wide temperature range. The χ'' maximum is visible up to 3.3 K in the 18.6 - 1000 Hz window and shows larger thermal shift above 2.5 K (Figure S11b and Table S8). Fitting of the temperature dependence of ln(τ) using Eq. 3 (see main text) with A and B_2 fixed based on the results of $\tau(H)$ dependence fitting, shows a significant contribution of the phonon bottle-neck process (C = 93(33) s$^{-1}\cdot$K^{-2}, n = 2.0(5)) and Orbach relaxation process (τ_0 = 6.0(15.2)$\cdot$10^{-10} s; U_{eff}/k_B = 41(8) K) (Figure 3f). All parameters obtained by fitting the respective relaxation rates vs magnetic field and temperature using Eqs 2 and 3 are collected in Table S9 and in Table 3 in the main text.

Table S8. Values of α and τ parameters with uncertainties provided in parentheses obtained from generalized Debye model fitting of the $\tau(v)$ dependences for **4** at 1.8 K in the 0.020-0.450 T magnetic field range (columns 1-5) and at 0.200 T measured at various temperatures in the 1.8-3.5 K range (columns 6-10).

	Figure S11a					Figure S11b			
	T = 1.8 K					H = 2000 Oe			
H (Oe)	χ_s (cm$^3\cdot$mol^{-1})	χ_t (cm$^3\cdot$mol^{-1})	α	τ (s)	T (K)	χ_s (cm$^3\cdot$mol^{-1})	χ_t (cm$^3\cdot$mol^{-1})	α	τ (s)
200	3.26(9)	4.93(2)	0.012(30)	1.97(14)$\cdot$10^{-4}	1.8	0.21(1)	2.80(2)	0.306(7)	16.9(3)$\cdot$10^{-4}
300	2.19(6)	4.78 (2)	0.069(16)	2.52(9)$\cdot$10^{-4}	1.9	0.21(2)	2.73(2)	0.319(9)	15.8(3)$\cdot$10^{-4}
400	1.48(4)	4.65(1)	0.132(9)	3.40(7)$\cdot$10^{-4}	2.0	0.23(2)	2.67(2)	0.310(10)	15.0(3)$\cdot$10^{-4}
500	1.05(3)	4.54(1)	0.172(7)	4.46(7)$\cdot$10^{-4}	2.1	0.23(1)	2.70(1)	0.318(6)	15.0(2)$\cdot$10^{-4}
600	0.78(3)	4.44(1)	0.200(6)	5.73(7)$\cdot$10^{-4}	2.3	0.24(2)	2.60(2)	0.296(8)	12.7(2)$\cdot$10^{-4}
800	0.47(2)	4.22(2)	0.241(6)	8.27(9)$\cdot$10^{-4}	2.5	0.26(2)	2.51(1)	0.261(7)	10.0(1)$\cdot$10^{-4}
1000	0.30(2)	4.03(2)	0.283(5)	10.9(1)$\cdot$10^{-4}	2.7	0.28(2)	2.36(1)	0.211(9)	6.71(11)$\cdot$10^{-4}
1500	0.21(1)	3.37(2)	0.310(5)	15.6(2)$\cdot$10^{-4}	2.9	0.25(4)	2.28(1)	0.194(15)	4.12(14)$\cdot$10^{-4}
2000	0.19(2)	2.77(3)	0.319(10)	16.9(4)$\cdot$10^{-4}	3.1	0.22(7)	2.20(2)	0.191(21)	2.36(15)$\cdot$10^{-4}
2500	0.18(1)	2.25(2)	0.308(8)	14.5(2)$\cdot$10^{-4}	3.3	0.19(17)	2.13 (2)	0.206(36)	1.28(21)$\cdot$10^{-4}
3000	0.19(2)	1.74(2)	0.260(14)	10.0(3)$\cdot$10^{-4}	3.5	-0.05(50)	2.06(2)	0.263(54)	0.54(25)$\cdot$10^{-4}
3500	0.15(2)	1.43(1)	0.277(17)	6.94(25)$\cdot$10^{-4}					
4000	0.022(82)	1.22(3)	0.371(46)	4.08(63)$\cdot$10^{-4}					
4500	-0.011(116)	1.00(3)	0.385(60)	2.41(68)$\cdot$10^{-4}					
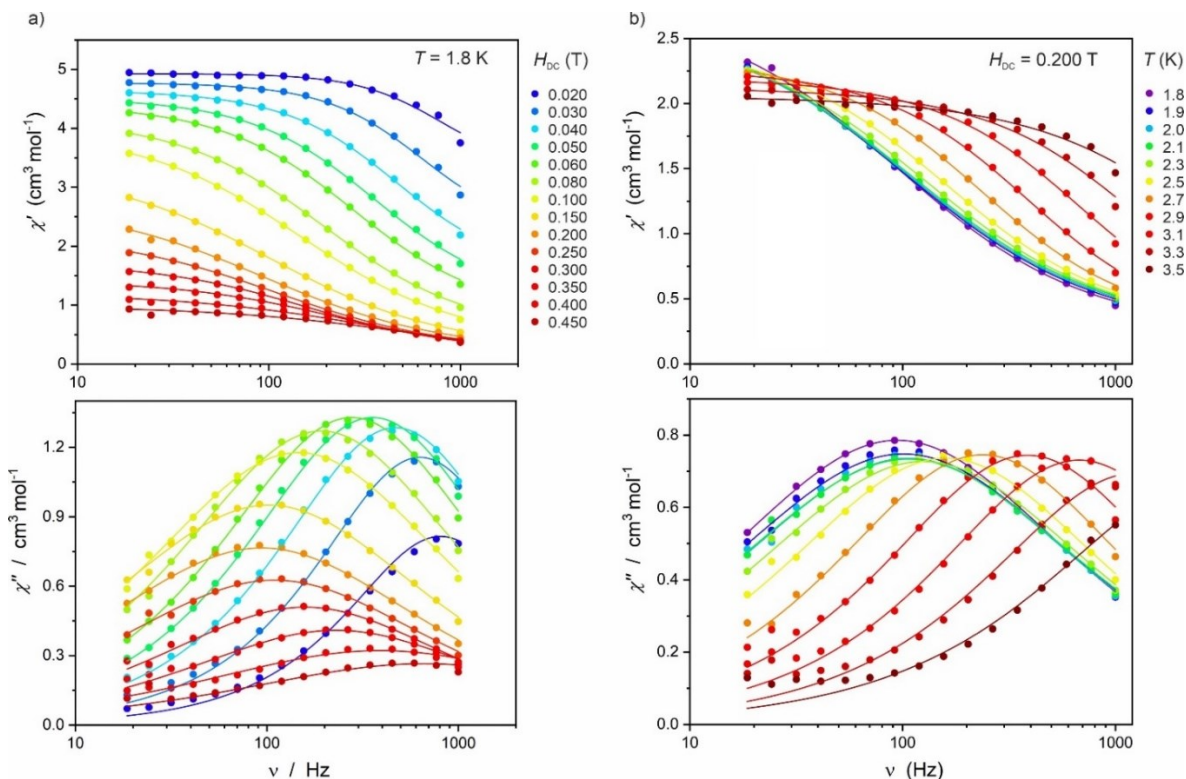
Figure S11. In-phase (χ') and out-of-phase (χ'') AC susceptibilities for **4** at 1.8 K measured in the 0.020-0.450 T magnetic field range (a) and at 0.200 T measured at various temperatures in the 1.8-3.5 K range (b). Values of α and τ parameters with uncertainties provided in parentheses are gathered in Table S8. The solid lines are the best fits to generalized Debye model.

Table S9. Values of the best-fit parameters obtained by fitting the $\tau(H)$ using Eq. 2 (top part) and the $\tau(T)$ using Eq. 3 (bottom part) for compound **4**. The relevant fits are shown in Figure 3e and 3f in the main text, respectively. This table is also included in Table 3 in the main text.

$$\tau^{-1}(H) = A_1/(1+A_2H^2) + B_1H^4 + D \qquad\qquad \text{(Eq. 2)}$$
$$\ln\tau(T^{-1}) = \ln[(A + B_2T + CT^n + \tau_0^{-1}\exp(-U_{eff}/k_BT))^{-1}] \qquad\qquad \text{(Eq. 3)}$$

T (K)	1.8
range (Hz)	18.6-1000
field range (Oe)	200-4500
A_1 (s^{-1})	7281(348)
A_2 (Oe^{-2})	1.13(7)$\cdot$10^{-5}
B_1 (Oe^{-4})	7.1(2)$\cdot$10^{-12}
D (s^{-1})	322(9)
R^2	0.99893
H_{DC} (T)	2000
range (Hz)	18.6-1000
temp. range (K)	1.8-3.5
A (s^{-1})	157.6 (fixed)
B_2 (s^{-1}K^{-1})	63.1 (fixed)
C (s^{-1}K^{-n})	93(33)
n	2.0(5)
τ_0 (s)	6.0(15.2)$\cdot$10^{-10}
(U_{eff}/k_B) (K)	41(8)
R^2	0.98322

Ab initio calculations

Ab initio calculations were carried out using the OpenMolcas quantum chemistry software package,[8] and were performed on experimental geometries taken from the single crystal X-ray diffraction analysis. For **3** two non-equivalent molecules denoted as **3A** and **3B** were considered, while for **1** and **4** only one molecule was taken for analysis. The fragments of crystal structure employed for analysis together with calculated main quantization axes (z) are presented in Figure 4. Two models with different basis sets were used: **S** - small with VDZP basis function quality for Er^{III} central ion and VDZ for other atoms and **L** – large with VTZP basis for Er^{III} and VDZP for atoms in the first coordination sphere together with Li ions. Table S10 contains contractions and labels of basis sets **S** and **L** for all atoms. The performed calculations were of CASSCF/RASSI/SINGLE_ANISO type.[9] Scalar relativistic effects were taken into account by employing second order DKH (Douglas-Kroll-Hess) Hamiltonian and relativistic basis sets of an ANO-RCC type. In order to save disk space, Cholesky decomposition of ERI-s (electron repulsion integrals) was used with the $1.0 \cdot 10^{-8}$ threshold. In the first step, a state average multi-configurational self-consistent field (SA-CASSCF) calculation for 35 quartets and 112 doublets rising from different Er^{III} configurations was carried out. The active space was composed out of seven f-orbitals with eleven active valence electrons – CAS(11in7). In the next step, all quartets and doublets optimized as spin-free states in CASSCF step were mixed by the spin-orbit coupling within RASSI (Restricted Active Space State Interaction Program) using mean-field spin-orbit (SO) integrals (AMFI) resulting in 364 spin-orbit states. In the final step, a SINGLE_ANISO module was used to decompose the spin-orbit states into states with a definite projection of the total momentum on the located quantization axis and to calculate crystal-field parameters of the Zero Field Splitting (ZFS) Hamiltonian within the manifold of $J = 15/2$ together with three components of the pseudo-g-tensor for eight ground Kramers doublets.[10] The obtained energy splitting of the $J = 15/2$ manifold, together with the g_x, g_y, g_z components of the pseudo-g-tensors within the basis of each doublet ($\tilde{S} = 1/2$) and decomposition of the ground state into states with a definite angular momentum on quantization axis are presented in Tables S11-S14. All 27 crystal-field parameters of rank k = 2, 4 and 6 were gathered in Tables S15-S17 together with their weights on the crystal field splitting. Magnetic transition moments between states for **1**, **3** and **4** are visualized in Figure 4 in the article. Comparison of the calculated $M(H)$ and $\chi T(T)$ dependencies (solid lines) with experimental ones (points) can be found in Figures S3, S5 and S6. The agreement between the calculated and experimental data is satisfactory.

Attempts to calculate the energy diagram and magnetic properties of **2** were unsuccessful due to the additional spin on the TEMPO ligand. However, in order to better understand the crystal field in **2**, we have replaced the N atom in TEMPO with the C atom so that the TEMPO has lost its radical character and the calculations were possible for such a modified model of **2** (Table S18 and S19).

Table S10. Description and contractions of the basis sets (two models: **S** - small, **L** - large) employed in *ab initio* calculations of the Er^{III} crystal field in **Er_ttbp** (compound **1**), **Er_bht_1** (compound **3**), **Er_bht_2** (compound **3**) and **Er_n3ncl2** Er_ttbp (compound **4**).

Basis set "S"	Basis set "L"
Er.ANO-RCC-VDZP 7S6P4D2F1G	Er.ANO-RCC-VTZP 8S7P5D3F2G1H
Li.ANO-RCC-VDZ 3S2P	Li.ANO-RCC-VDZP 3S2P1D
Cl.ANO-RCC-VDZ 4S3P	Cl.ANO-RCC-VDZP 4S3P1D
Si.ANO-RCC_VDZ 4S3P	Si.ANO-RCC_VDZ 4S3P
N.ANO-RCC-VDZ 3S2P	N.ANO-RCC-VDZP 3S2P1D
O.ANO-RCC-VDZ 3S2P	O.ANO-RCC-VDZ 3S2P (distant atoms in Er_n3ncl2) O.ANO-RCC-VDZP 3S2P1D (first coordination sphere in Er_bht)
C.ANO-RCC-VDZ 3S2P	C.ANO-RCC-VDZ 3S2P
H.ANO-RCC-VDZ 2S	H.ANO-RCC-VDZ 2S

Table S11. Summary of the energy splitting of the $^4I_{15/2}$ multiplet of Er^{III} in compound **1** with pseudo-*g*-tensors of each Kramers doublet and the composition of the ground state in $|m_J\rangle$ basis.

Compound **1**							
S				L			
Energy and Pseudo-*g*-tensor components **(g_x, g_y, g_z) of 8 ground Kramers doublets**							
Energy / cm^{-1}	Pseudo-*g*-tensor components			Energy / cm^{-1}	Pseudo-*g*-tensor components		
	g_x	g_y	g_z		g_x	g_y	g_z
0.000	0.0166	0.0261	17.6511	0.000	0.0070	0.0129	17.6548
99.740	0.2645	0.6156	14.2647	104.431	0.0670	0.1459	14.8648
140.763	0.5799	1.1535	15.9697	156.372	0.5801	1.3121	15.2402
162.438	1.2964	3.3779	10.0513	176.619	0.6328	2.5562	10.1457
226.866	7.7119	6.3032	2.6093	241.634	7.0440	6.5546	2.9839
317.568	2.1591	4.0788	8.2183	330.470	0.9440	4.0624	8.7756
371.244	2.3020	3.6540	11.2772	388.376	2.1676	2.7734	11.3834
423.222	0.4566	1.6293	16.2343	439.286	0.4359	1.5891	15.8730
Composition of ground Kramers doublet in the $\lvert m_J\rangle$ basis on the quantization axis of the ground doublet within J = 15/2 manifold							
90.0% $\lvert +15/2\rangle$ 5.9% $\lvert -15/2\rangle$ 2.0% $\lvert +11/2\rangle$ 1.3% $\lvert +9/2\rangle$ 0.3% $\lvert +7/2\rangle$ 0.2% $\lvert +13/2\rangle$				65.4% $\lvert +15/2\rangle$ 30.3% $\lvert -15/2\rangle$ 1.8% $\lvert +11/2\rangle$ 0.8% $\lvert -11/2\rangle$ 0.8% $\lvert +9/2\rangle$ 0.4% $\lvert -9/2\rangle$			

Table S12. Summary of the energy splitting of the $^4I_{15/2}$ multiplet of Er^{III} in compound **3** molecule **A** model with pseudo-*g*-tensors of each Kramers doublet and the composition of the ground state in $|m_J\rangle$ basis.

3A							
S				L			
Energy and Pseudo-*g*-tensor components (g$_x$, g$_y$, g$_z$) of 8 ground Kramers doublets							
Energy / cm^{-1}	Pseudo-*g*-tensor components			Energy / cm^{-1}	Pseudo-*g*-tensor components		
	g$_x$	g$_y$	g$_z$		g$_x$	g$_y$	g$_z$
0.000	0.0063	0.0101	17.4817	0.000	0.0047	0.0082	17.4996
89.941	0.1155	0.1614	14. 8081	95.310	0.1209	0.1622	14.9565
143.673	0.2858	0.4257	15.4163	155.664	0.4379	0.6353	14.5597
166.980	0.5369	1.1325	10.6607	180.602	0.5652	1.2815	11.0978
226.748	3.8524	4.7912	7.3881	239.456	3.4272	4.6192	7.4037
301.051	0.7321	4.0036	9.1724	309.892	1.7007	3.8112	9.7762
361.458	1.5917	2.4556	11.9526	375.625	1.2780	2.0367	12.6439
419.942	0.3034	1.0719	16.0860	444.682	0.1960	0.6264	16.3898
Composition of ground Kramers doublet in $|m_J\rangle$ basis on the quantization axis within J = 15/2 manifold							
85.9% $\|+15/2\rangle$ 5.7% $\|-15/2\rangle$ 6.2% $\|+11/2\rangle$ 1.0% $\|+9/2\rangle$ 0.5% $\|+13/2\rangle$				92.0% $\|+15/2\rangle$ 6.5% $\|+11/2\rangle$ 1.0% $\|+9/2\rangle$ 0.4% $\|+13/2\rangle$			

Table S13. Summary of the energy splitting of the $^4I_{15/2}$ multiplet of Er^{III} in compound **3** molecule **B** with pseudo-*g*-tensors of each Kramers doublet and the composition of the ground state in $|m_J\rangle$ basis.

3B							
S				L			
Energy and Pseudo-*g*-tensor components (g$_x$, g$_y$, g$_z$) of 8 ground Kramers doublets							
Energy / cm^{-1}	Pseudo-*g*-tensor components			Energy / cm^{-1}	Pseudo-*g*-tensor components		
	g$_x$	g$_y$	g$_z$		g$_x$	g$_y$	g$_z$
0.000	0.0013	0.0049	17.2398	0.000	0.0008	0.0016	17.2563
94.418	0.0628	0.0913	14.2288	97.853	0.0806	0.1074	14.4333
158.601	0.1230	0.1888	17.4167	170.528	0.4235	0.6012	15.2183
172.526	0.5288	0.8592	10.4274	183.870	0.6178	1.2536	10.7061
236.249	3.9879	4.4280	7.7190	246.739	3.3865	4.4526	7.5997
312.298	0.3023	3.7431	9.2701	320.790	1.0493	3.7491	9.2548
373.865	1.6225	2.3838	12.5233	385.778	1.5180	2.2695	12.9284
430.487	0.3901	1.4739	16.0180	455.491	0.2613	0.8915	16.3942
Composition of ground Kramers doublet in $|m_J\rangle$ basis on the quantization axis within J = 15/2 manifold							
69.6% $\|+15/2\rangle$ 17.0% $\|-15/2\rangle$ 6.9% $\|+11/2\rangle$ 1.7% $\|+9/2\rangle$ 1.8% $\|+13/2\rangle$				85.3% $\|+15/2\rangle$ 1.6% $\|-15/2\rangle$ 9.0% $\|+11/2\rangle$ 1.6% $\|+9/2\rangle$ 1.8% $\|+13/2\rangle$			

Table S14. Summary of the energy splitting of the $^4I_{15/2}$ multiplet of Er^{III} in compound **4** with pseudo-g-tensors of each Kramers doublet and the composition of the ground state in $|m_J\rangle$ basis.

Compound **4**							
S				L			
Energy and Pseudo-g-tensor components							
(g_x, g_y, g_z) of 8 ground Kramers doublets							
Energy / cm^{-1}	Pseudo-g-tensor components			Energy / cm^{-1}	Pseudo-g-tensor components		
	g_x	g_y	g_z		g_x	g_y	g_z
0.000	0.0358	0.0824	16.4810	0.000	0.0480	0.1031	16.4440
39.535	0.0067	0.1101	12.8726	30.556	0.0296	0.1454	12.7906
101.488	2.3153	2.3826	9.0310	89.274	1.7998	1.9254	8.9212
155.009	4.0910	5.7441	8.3308	140.862	4.7443	5.2939	8.8112
217.760	0.0350	2.3700	13.5905	223.688	2.2751	5.3122	8.9437
256.080	0.8858	1.8978	13.8751	249.360	1.7824	5.1874	10.5539
308.850	0.0672	0.8419	16.5299	280.533	0.0887	0.9437	16.3007
338.370	0.0858	0.8477	16.7534	331.665	0.1312	0.4231	17.1844
Composition of ground Kramers doublet in $|m_J\rangle$ **basis on the quantization axis within J = 15/2 manifold**							
40.5% $\vert +15/2\rangle$ 23.6% $\vert -15/2\rangle$ 12.1% $\vert +13/2\rangle$ 7.3% $\vert +11/2\rangle$ 7.0% $\vert -13/2\rangle$ 4.1% $\vert -11/2\rangle$ 2.6% $\vert +9/2\rangle$ 1.8% $\vert -9/2\rangle$				31.5% $\vert +15/2\rangle$ 31.5% $\vert -15/2\rangle$ 9.9% $\vert +13/2\rangle$ 9.9% $\vert -13/2\rangle$ 6.1% $\vert -11/2\rangle$ 5.8% $\vert -11/2\rangle$ 2.3% $\vert -9/2\rangle$ 1.8% $\vert +9/2\rangle$			

Table S15. Crystal-field parameters, B_k^q (k = 2, 4, 6) of Er^{III} complexes defined in ref. 6 for **1** in the basis set **L** model obtained using *ab initio* calculations without symmetry constrains and their weights on crystal field splitting in descending order.

		1 in the basis set **L**	
k	q	B_k^q	Weight / %
2	0	-2.07E+00	20.78996
4	-1	-4.76E-03	8.669356
2	-1	7.66E-01	7.688352
4	3	3.20E-03	5.8338
4	-4	-3.10E-03	5.657771
2	2	4.79E-01	4.812641
6	-4	2.48E-05	4.230257
4	-3	2.28E-03	4.158291
6	2	-2.05E-05	3.500833
4	-2	-1.75E-03	3.191822
6	-6	1.83E-05	3.122037
6	-1	1.73E-05	2.959918
2	1	2.85E-01	2.861501
6	0	-1.61E-05	2.758342
4	4	1.34E-03	2.449922
6	5	1.38E-05	2.360959
6	3	-1.35E-05	2.311446
2	-2	-2.23E-01	2.240751
4	2	-1.11E-03	2.017328
6	1	-1.14E-05	1.942748
6	-3	8.94E-06	1.527337
4	0	5.77E-04	1.051771
6	6	-5.48E-06	0.935984
6	4	-4.65E-06	0.795128
4	1	-3.95E-04	0.720651
6	-5	-3.93E-06	0.671304
6	-2	1.28E-06	0.218606

Table S16. Crystal-field parameters, B_k^q (k = 2, 4, 6) of Er^{III} complexes defined in ref. 6 for **3A** and **3B** in the basis set **L** models obtained using *ab initio* calculations without symmetry constrains and their weights on crystal field splitting in descending order.

		3A in the basis set **L**				**3B** in the basis set **L**	
k	q	B_k^q	Weight / %	k	q	B_k^q	Weight / %
2	0	-2.05E+00	21.58893	2	0	-2.09E+00	20.62163
4	1	3.93E-03	7.506708	4	1	4.68E-03	8.401507
2	1	-6.50E-01	6.849065	4	3	4.01E-03	7.188348
4	3	-3.54E-03	6.767693	6	-2	-3.96E-05	6.668036
2	2	6.17E-01	6.503988	2	1	-6.73E-01	6.651333
4	4	-3.00E-03	5.739744	4	-4	-2.79E-03	5.002434
2	-1	5.23E-01	5.506405	6	3	-2.55E-05	4.28814
4	-1	-2.63E-03	5.023797	2	-2	-4.14E-01	4.091854
4	2	2.24E-03	4.291609	4	-1	-2.08E-03	3.728592
6	3	2.15E-05	3.863424	6	4	-1.98E-05	3.328073
6	-2	-2.15E-05	3.85813	6	2	1.75E-05	2.950623
6	0	-1.67E-05	3.002886	4	-3	-1.56E-03	2.806738
6	-6	1.52E-05	2.723784	6	-3	-1.55E-05	2.61578
6	1	-1.31E-05	2.344341	4	0	1.27E-03	2.285823
6	-3	-1.19E-05	2.141282	6	0	-1.31E-05	2.21176
4	0	1.07E-03	2.051036	4	-2	-1.01E-03	1.816397
6	4	1.09E-05	1.954757	6	-6	-9.79E-06	1.648233
6	2	1.05E-05	1.874179	6	6	-9.51E-06	1.599897
6	5	8.36E-06	1.498308	4	2	-8.90E-04	1.596598
6	6	-7.91E-06	1.417589	4	4	8.24E-04	1.479102
4	-3	-5.50E-04	1.052509	6	5	8.61E-06	1.448428
6	-4	-3.96E-06	0.709288	2	-1	1.35E-01	1.337194
6	-1	-2.36E-06	0.422403	6	-5	7.91E-06	1.330937
2	-2	-3.80E-02	0.400401	6	-1	7.37E-06	1.240784
4	-2	1.25E-04	0.239689	2	2	-1.23E-01	1.220135
4	-4	-8.61E-05	0.164654	6	-4	6.57E-06	1.105149
6	-5	-3.88E-07	0.069491	6	1	-4.20E-06	0.706008

Table S17. Crystal-field parameters, B_k^q (k = 2, 4, 6) of Er^{III} complexes defined in ref. 6 for **4** in the basis set **L** model obtained using *ab initio* calculations without symmetry constrains and their weights on crystal field splitting in descending order.

		4 in the basis set L	
k	q	B_k^q	Weight / %
4	-1	-7.40E-03	14.47472
2	0	-1.01E+00	10.86274
6	2	-5.41E-05	9.924257
4	-4	4.73E-03	9.246317
6	3	-4.93E-05	9.045388
6	-2	-4.66E-05	8.550529
6	5	-3.89E-05	7.131003
6	-3	2.91E-05	5.342933
4	1	2.62E-03	5.129553
4	4	1.75E-03	3.424274
4	0	1.33E-03	2.603503
4	-2	-1.09E-03	2.130787
4	2	-7.79E-04	1.522168
2	2	1.30E-01	1.404634
6	-4	6.89E-06	1.263064
6	-1	6.22E-06	1.141012
4	-3	-5.22E-04	1.020338
2	-1	-9.38E-02	1.010148
6	1	4.71E-06	0.863375
6	-5	4.26E-06	0.781522
6	0	3.71E-06	0.680811
2	-2	4.78E-02	0.51449
4	3	1.95E-04	0.381768
6	-6	-1.83E-06	0.335396
2	1	9.92E-03	0.106921
6	6	-1.72E-07	0.031494
6	4	1.71E-07	0.03137

Table S18. Summary of the energy splitting of the $^4I_{15/2}$ multiplet of Er^{III} in a modified model of compound **2** (N-atom of the TEMPO replaced by C-atom) with pseudo-*g*-tensors of each Kramers doublet and the composition of the ground state in $|m_J\rangle$ basis.

Modified model of compound **2**							
S				**L**			
Energy and Pseudo-*g*-tensor components (g_x, g_y, g_z) of 8 ground Kramers doublets							
Energy / cm^{-1}	Pseudo-*g*-tensor components			Energy / cm^{-1}	Pseudo-*g*-tensor components		
	g_x	g_y	g_z		g_x	g_y	g_z
0.000	0.0363	0.1047	16.5251	0.000	0.0362	0.0611	17.2833
28.678	0.0286	0.1235	15.7704	43.882	0.0359	0.0905	16.4814
93.649	0.2365	0.3003	15.4267	101.200	0.3429	0.4377	14.8384
120.374	1.1035	1.3877	10.4748	138.069	1.1025	1.3779	11.0316
170.974	3.9208	4.8550	6.9869	185.379	4.0245	4.9822	6.4596
241.144	0.5377	3.3337	8.1177	257.340	0.2519	3.1021	8.4893
285.345	1.2909	4.4076	11.8418	308.092	1.1303	3.5089	12.5626
426.301	0.0306	0.0633	17.5141	459.700	0.0281	0.0602	17.5406
Composition of ground Kramers doublet in the $|m_J\rangle$ basis on the quantization axis of the ground doublet within J = 15/2 manifold							
69.4% $\|+15/2\rangle$ 14.1% $\|+13/2\rangle$ 7.0% $\|+11/2\rangle$ 6.6% $\|+9/2\rangle$ 1.6% $\|+7/2\rangle$ 0.5% $\|-15/2\rangle$				85.1% $\|+15/2\rangle$ 4.1% $\|-15/2\rangle$ 4.1% $\|+11/2\rangle$ 2.9% $\|+9/2\rangle$ 1.8% $\|+13/2\rangle$ 1.1% $\|+7/2\rangle$			

Table S19. Crystal-field parameters, B_k^q (k = 2, 4, 6) of Er^{III} complexes defined in ref. 6 for a modified model of **2** (N-atom of the TEMPO replaced by C-atom) in the basis set **L** obtained using *ab initio* calculations without symmetry constrains and their weights on crystal field splitting in descending order.

		modified **2** in the basis set L	
k	q	B_k^q	Weight / %
2	0	-1.63E+00	14.10893
2	2	1.40E+00	12.11048
4	-1	-5.73E-03	8.999707
2	-1	9.82E-01	8.494804
4	4	4.68E-03	7.351983
2	-2	-8.40E-01	7.267856
6	2	-3.48E-05	5.125603
4	-4	-2.62E-03	4.110489
6	-4	2.64E-05	3.887397
6	-6	-2.07E-05	3.04814
4	3	1.77E-03	2.774343
4	-3	1.75E-03	2.741114
6	1	-1.71E-05	2.513217
2	1	2.79E-01	2.408999
6	5	1.37E-05	2.011658
6	0	-1.34E-05	1.979419
6	4	-1.29E-05	1.894171
6	-1	1.25E-05	1.839754
4	-2	1.01E-03	1.578217
6	6	9.61E-06	1.414427
4	2	-7.80E-04	1.223706
6	-3	4.85E-06	0.71395
4	0	3.81E-04	0.598206
6	-5	3.41E-06	0.501326
6	3	2.59E-06	0.380612
6	-2	1.17E-06	0.171642
4	1	6.51E-05	0.102138

References

1. C. C. Cummins, R. R. Schrock, W. M. Davis, *Inorg. Chem.* 1994, **33**, 1448–1457

2. F. Yuan, J. Yang, L. Xiong, *J. Organomet. Chem.* 2006, **691**, 2534-2539

3. G. M. Sheldrick, *Acta Crystallogr. C*, 2015, **71**, 3–8

4. O. V Dolomanov, L. J. Bourhis, R. J. Gildea, J. A. K. Howard and H. Puschmann, *J. Appl. Crystallogr.*, 2009, **42**, 339–341

5. M. Arczyński, J. Stanek, B. Sieklucka, K. R. Dunbar and D. Pinkowicz, *J. Am. Chem. Soc.*, 2019, **141**, 19067–19077

6. L. Gu, R. Wu, *Phys. Rev. B*, 2021, **103**, 014401

7. K. N. Shrivastava, *Phys. Stat. Sol. B*, 1983, **117**, 437-458

8. I. F. Galvam, M. Vacher, A. Alavi, C. Angeli, F. Aquilante, J. Autschbach, J. J. Bao, S. I. Bokarev, N. A. Bogdanov, R. K. Carlson, L. F. Chibotaru, J. Creutzberg, N. Dattani, M. G. Delcey, S. S. Dong, A. Dreuw, L. Freitag, L. M. Frutos, L. Gagliardi, F. Gendron, A. Giussani, L. Gonzalez, G. Grell, M. Guo, C. E. Hoyer, M. Johansson, S. Keller, S. Knecht, G. Kovacevic, E. Kallman, G. L. Manni, M. Lundberg, Y. Ma, S. Mai, J. P. Malhado, P. A. Malmqvist, P. Marquetand, S. A. Mewes, J. Norell, M. Olivucci, M. Oppel, Q. M. Phung, K. Perloot, F. Plasser, M. Reiher, A. M. Sand, I. Schapiro, P. Sharma, C. J. Stein, L. K. Sorensen, D. G. Truhlar, M. Ugandi, L. Ungur, A. Valentini, S. Vancoillie, V. Veryazov, O. Weser, T. A. Wesołowski, P.-O. Widmark, S. Wouters, A. Zech, J. P. Zobel, R. Lindh, *J. Chem. Theory Comput.* 2019, **15**, 5925–5964

9. L. F. Chibotaru, L. Ungur, *J. Chem. Phys.* 2012, **137**, 064112

10. L. Ungur, L. F. Chibotaru, *Chem. Eur. J.* 2017, **23**, 3708–3718